processes

MDPI

Article

Chloride-Derived Bimetallic Cu-Fe Nanoparticles for High-Selective Nitrate-to-Ammonia Electrochemical Catalysis

Zixuan Tang [1], Zehui Bai [1], Xin Li [1], Le Ding [1], Bin Zhang [1] and Xinghua Chang [1,2,*]

[1] School of Minerals Processing and Bioengineering, Central South University, Changsha 410083, China; tangzx0305@163.com (Z.T.); 18477161975@163.com (Z.B.); 215612079@csu.edu.cn (X.L.); ding1430477283@163.com (L.D.); 8204192610@csu.edu.cn (B.Z.)

[2] Key Laboratory for Mineral Materials and Application of Hunan Province, Central South University, Changsha 410083, China

* Correspondence: changxinghua@csu.edu.cn

Abstract: Cu-based bimetallic materials have been widely reported as efficient catalysts for electrocatalytic nitrate reduction. However, the faradaic efficiency and selectivity are still far from satisfactory. Herein, Cu-Fe bimetallic nanoalloys with adjustable Cu/Fe ratios are successfully prepared through a reactive mechanical milling approach with $CuCl_2$, $FeCl_3$ and Na as the starting materials. The optimized Cu_3Fe exhibits excellent nitrate conversion efficiency of 81.1% and 70.3% ammonia selectivity at −0.7 V vs. RHE within 6 h under 0.1 M Na_2SO_4 and 100 ppm NO_3^-. The Fe-introduction-induced upshift of the *d*-band center is identified to be beneficial for promoting nitrate adsorption on Cu_3Fe. Moreover, favorable H generation under the assistance of Fe could effectively accelerate the stepwise hydrogenation during electrocatalytic nitrate reduction, resulting in significantly improved NH_4^+ selectivity. This work supplies valuable insights for the rational design of transition-metal-based bimetallic catalysts for electrocatalytic nitrate reduction.

Keywords: Cu-Fe bimetallic catalysts; nitrate to ammonia; *d*-band center regulation

check for updates

Citation: Tang, Z.; Bai, Z.; Li, X.; Ding, L.; Zhang, B.; Chang, X. Chloride-Derived Bimetallic Cu-Fe Nanoparticles for High-Selective Nitrate-to-Ammonia Electrochemical Catalysis. *Processes* **2022**, *10*, 751. https://doi.org/10.3390/pr10040751

Academic Editor: Enrico Marsili

Received: 17 March 2022
Accepted: 31 March 2022
Published: 13 April 2022

Publisher's Note: MDPI stays neutral with regard to jurisdictional claims in published maps and institutional affiliations.

Copyright: © 2022 by the authors. Licensee MDPI, Basel, Switzerland. This article is an open access article distributed under the terms and conditions of the Creative Commons Attribution (CC BY) license (https://creativecommons.org/licenses/by/4.0/).

1. Introduction

Intensified industrialization breaks the global nitrogen cycle, resulting in concentrated nitrate in groundwater and other water bodies [1]. Excessive nitrate discharge always leads to severe environmental contamination and impending threat to public health [2,3]. To address the nitrate contamination and restore the nitrogen cycle in nature, several physicochemical and biological approaches have been commercially applied [4,5]. Although nitrate enrichment could be successfully achieved based on physicochemical strategies, subsequent hazard-free treatment is still mandatorily required, which always involves complex procedures with high costs. The microbial approach always suffers from long process flow and poor resistance to environmental disturbance. Therefore, developing highly efficient, stable and cost-effective alternative strategies to achieve nitrate removal is of great significance for water restoration. In this context, electrocatalytic nitrate reduction is attracting intensive attention due to its ability to apply external circuit current rather than chemical agents as an electron donor to reduce nitrate. The booming green energy systems enable the electrochemical reduction of nitrate to be more eco-friendly and cost-effective. In addition, electrocatalytic denitrification exhibits a strong anti-interference capability to adapt to environmental fluctuation. Thus, compared with physicochemical and biological approaches, the electrochemical strategy is more efficient, stable and flexible for nitrate removal.

Recently, intensive studies have focused on electrocatalytic reduction of nitrate into NH_4^+, which exhibits the potential to replace or at last supplement the energy-intensive Haber-Bosch process for NH_3 production. However, achieving high selectivity toward

the desirable NH_4^+ is still challenging due to the sluggish reaction kinetics involving complex proton-electron coupled reactions. In addition, the possible generation of various N-containing by-products further aggravates the complexity of electrocatalytic denitrification. Therefore, developing highly efficient catalysts with rationally designed structures is of great significance for achieving high efficient electroreduction of nitrate with outstanding ammonia selectivity, which can be further regarded as NO_3RR to ammonia (NRA) process. By consensus, precious metal-based materials are novel catalysts for driving NRA [6] but are restricted by limited reserves and high prices, cost-effective non-noble metal catalysts are more desirable for practical application. Among them, Cu-based materials have attracted intensive research interest as promising catalysts for RNA. It has been proved that metallic Cu could efficiently capture O atoms from nitrate, promoting cleavage of N-O bond to form nitrite [7]. Nevertheless, further breaking the N-O bond in nitrite under the assistance of Cu is inefficient because of the weak adsorption capacity for the nitrite intermediate [8,9]. As is well known, the electroreduction of nitrate involves complex proton-coupled electron transfer (PCET) reactions, while Cu exhibits poor catalytic properties for H atom evolution [7], resulting in limited PCET efficiency. Therefore, monometallic Cu is insufficient to meet the requirements of achieving excellent nitrate removal performance with high NH_4^+ selectivity. According to the previous reports [10,11], Fe is proved to play a vital role in nitrate reduction. Fe-based catalysts have already been applied to the commercial Haber–Bosch process due to their appropriate binding energies with N-containing species [12]. Moreover, Fe is also confirmed to be a sufficient component for hydrogen evolution, and its adsorption capacity for H exceeds that of Pd [7], which is conducive to accelerating the stepwise PCET reaction during NRA. Therefore, it is expected that the bimetallic combination of Cu and Fe has great potential to enable an efficient and reliable NRA process with high selectivity towards NH_4^+. However, the intrinsic difference in redox potential leads to a severe challenge for the preparation of Cu-Fe nanoalloys.

In this study, Bimetallic Cu-Fe nanoparticles are successfully obtained simply through reactive mechanical milling. Different from traditional ball milling, reactive mechanical milling combines in-situ reduction and alloying reactions with $CuCl_2$ and $FeCl_3$ applied as metal sources and sodium as reducing agent. More importantly, reactive mechanical milling can conveniently adjust the Cu/Fe ratio by changing the ratio of metal sources without dealing with the redox potential differences, which is considered a difficulty in the electrodeposition method. The prepared Cu_3Fe catalyst presents 81.1% conversion of nitrate in 6 h with 70.3% ammonia selectivity and shows great catalytic performance retention after 5 catalysis cycles.

2. Experimental

2.1. Materials

Anhydrous ferric chloride ($FeCl_3$, 99.5%), Anhydrous copper trichloride ($CuCl_2$, 99.0%), Sodium metal (Na, 99.7%) were obtained from Aladdin Reagent Co., Ltd. (Shanghai, China). Absolute ethanol (CH_3CH_2OH, ≥99.7%) was obtained from Huihong Chemical Reagent Co., Ltd. (ChangSha, China). Concentrated hydrochloric acid (HCl, 38%) was obtained from Sinopharm Chemical Reagent Co., Ltd. (Shanghai, China). Nafion D-520 ($C_9HF_{17}O_5S$, 5 wt%) is obtained from DuPont Co., Ltd. (Minneapolis, MN, USA). All reagents were used directly without any further purification. The deionized water (DI-water) used in all experiments was purified by the QQ-UP20-W in the laboratory.

2.2. Preparation of Cu-Fe Nanoparticles

Cu-Fe nanoparticles were synthesized by a typical reactive mechanical milling method [13]. 60 g zirconia grinding beads of 3 different sizes was added into an airtight milling vessel. A certain amount of anhydrous ferric chloride, anhydrous copper chloride and sodium metal with a 10% excess amount was added into the milling vessel in the glove box. Then, the milling vessel was put back to the machine to carry out a 6 h reactive mechanical milling process.

After mechanical milling, 50 mL absolute ethanol was added into the milling vessel and stirred to remove unreacted metal sodium. Centrifuges were used to separate the remaining particles. In this step, no deionized water was added to avoid the reaction between Na and H_2O to form NaOH and further react with Fe in the bimetallic nanoparticle. Subsequently, 50 mL deionized water was added into the centrifugal tube, stirred and centrifuged to remove NaCl wrapped on catalyst particles. To obtain pure alloy nanoparticle sediment, repeated washing operations were necessary. Finally, the centrifugal tube with catalyst was freeze-dried for 10 h to avoid intense nanoparticle agglomeration during the evaporation process. The Cu catalyst was synthesized according to the same steps described above without adding $FeCl_3$.

2.3. Instrumentation

X-ray diffraction (XRD) patterns were taken on a TD-3500 diffractometer (Dandong Tongda, Dandong, China) using Cu Kα radiation (λ = 1.54056 Å) at 40 kV and 40 mA and collected in the 2θ range 3–80°. Energy-dispersive X-ray spectroscopy (EDS) analysis coupled to Scanning Electron Microscopy (SEM) was conducted on a MIRA3 instrument (TESCAN, Prague, Czech Republic). Transmission Electron Microscope (TEM) images were taken on a JEM-2100-F instrument (JEOL, Tokyo, Japan). X-ray photoelectron spectra (XPS) and ultraviolet photo-electron spectroscopy (UPS) were measured by an ESCALAB 250Xi Multi Technique System (Thermo Fisher, Waltham, MA, USA) equipped with an Al Kα X-ray exciting source (1486.6 eV). The binding energies were calibrated by using the C 1 s peak at 284.8 eV as an internal standard. UV–Vis spectra were obtained from a Unico 2800 spectrophotometer (Thermo Fisher, Waltham, MA, USA) with 1 cm quartz cells.

2.4. Concentration Detection for NO_3^-, NO_2^- and NH_4^+ by UV–Vis Spectrometry

A CuFe nanoparticle was deposited in Ni foam supports using Nafion as a binder to investigate product distribution in a catalysis cycle. NO_3^-, NO_2^-, and NH_4^+ concentration was recorded as a function of Cu/Fe ratio and reaction time. The characteristic absorption peak of NO_3^-, NO_2^- and NH_4^+ was identified and the corresponding standard curve was prepared (Figure S1) to detect the concentration. The concentration of NH_4^+ in the solution was detected by salicylic acid spectrophotometry, and deionized water was used as the background. The concentration of NO_2^- was detected by diazotization coupling spectrophotometry, and deionized water was used as the background. NO_3^- was simply detected by ultraviolet spectrophotometry, and for the NO_3^- characteristic absorption peak that could be detected at 220 nm without adding any chromogenic agent, 0.5 mL 1 M HCl was added to shield the interference from a characteristic absorption peak of CO_2 dissolved in the solution; 0.5 mL 1 M HCl was also added to the deionized water as the background. All the ion concentrations we detected were diluted to the corresponding linear area to fit their standard curve. Before electrolysis, argon was introduced into the electrolytic cell for 20 min to replace dissolved O_2. After that, the initial electrolyte sample was detected, and the electrolyte sample was detected every 2 h to track the product concentration variation.

2.5. Electrocatalytic Measurement of Nitrate Reduction

The cyclic voltammetry (CV) test of Cu-Fe nanoparticles with different Cu-Fe ratios was carried out to observe the electrocatalytic reaction process at different voltages. CV test was carried out in a three-electrode system: platinum wire electrode as a counter electrode; Ag/AgCl electrode as a reference electrode; a glassy carbon electrode coated with catalyst as a working electrode; 0.007 M $NaNO_3$ and 0.1 M Na_2SO_4 solution as electrolyte. All the potentials recorded were converted into the potential versus the reversible hydrogen electrode (RHE) during the CV test, and the scan rate of each test as set as 10 mV s^{-1}. Before the CV test, the electrode material was subjected to 3 cycles of CV scanning within the working voltage range to activate the electrode material, and then the CV test was carried out and recorded.

Koutecký–Levich (K-L) plots were obtained by linear sweep voltammetry (LSV) carried out on rotating disk electrode (RDE) at different rotation speeds. We used the K-L equation and K-L plots to calculate the number (n) of transferred electrons in the NRA reaction process.

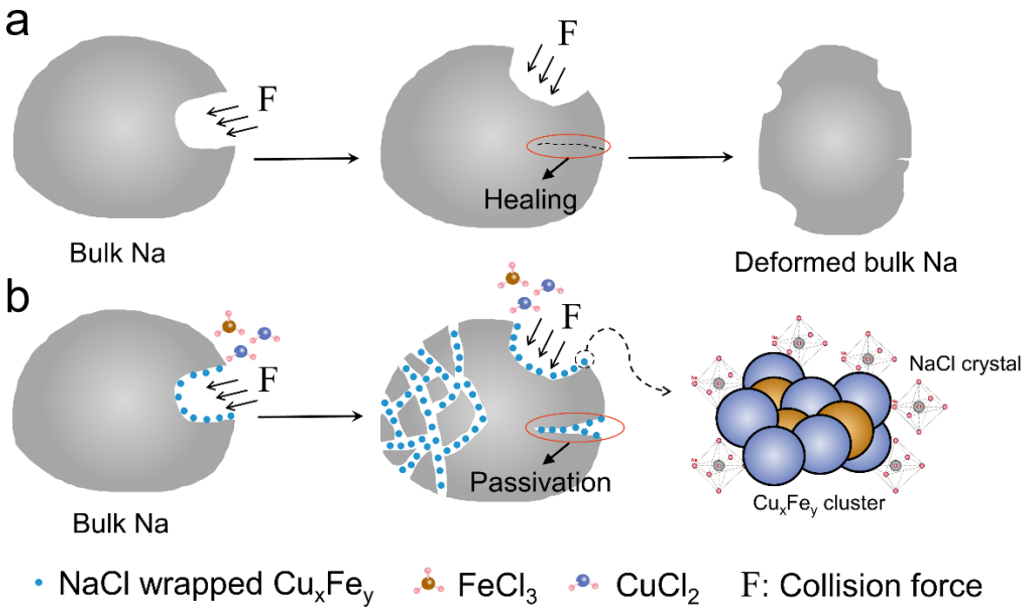
K-L analyses were performed according to the following K-L equation:

$$\frac{1}{i_m} = \frac{1}{i_K} + \frac{1}{0.62AnFD^{2/3}\nu^{-1/6}C\omega^{1/2}} \quad (1)$$

where A is the electrode area; i_m is the measured current; i_K is the kinetic current from NO_3^- electroreduction; n is the number of electron transfers in the reaction; F is Faraday's constant (96,485 C mol^{-1}); D represents the effective diffusion coefficient of nitrate, which is 1.4 × 10^{-5} cm^2 s^{-1} for 0.1 M nitrate at 25 °C; ν is the kinematic viscosity of water at 25 °C (1 × 10^{-6} m^2 s^{-1}); C is the nitrate concentration, and ω represents the electrode's rate of rotation (rpm).

3. Results and Discussion

As shown in Scheme 1, the Cu-Fe nanoalloys with different Cu/Fe ratios of 3:1, 1:1 and 1:3, donated as Cu_3Fe, CuFe and $CuFe_3$, respectively, are successfully achieved through changing the $CuCl_2/FeCl_3$ ratio during reactive mechanical milling. The phase structure of the as-prepared Cu-Fe nanoalloys is characterized by powder X-ray diffraction (XRD). As shown in Figure 1d, clear diffraction peaks centered at 43.4° and 50.5° are well resolved in Cu_3Fe, corresponding to the plane (111) and plane (200) of cubic Cu (JCPDS No. 04-0836), a 0.2° negative shift appeared on Cu (111) characteristic peaks suggesting the successful fabrication of Cu-Fe nanoalloy. In addition, another peak located at 44.6° can be indexed to Fe (101) (JCPDS No. 50-1275). With the content increase of $FeCl_3$ during mechanical milling, a sharp peak intensity decrease of cubic Cu takes place, combined with a rapid peak increase of Fe (101). Noteworthily, there is no intermetallic compound between Cu and Fe according to the corresponding phase diagram; thus, the as-prepared Cu-Fe nanoalloys were speculated mainly to exist in the form of a solid solution state. Morphology of the samples was investigated via scanning electron microscopy (SEM) and transmission electron microscopy (TEM). As shown in Figure S2, all the samples appear in the form of slightly aggregated particles of about 100 nm. Magnified TEM image further reveals that the aggregated particles are composed of nanoparticles 10 nm in diameter (Figure 1a,b). Furthermore, the distinct clear lattice spacing of 0.209 nm for the Cu (111) plane of Cu_3Fe is well resolved [14] (Figure 1b), which is 1% larger than that of pure Cu, indicating lattice stretching of Cu (111) by Fe doping. Also, the distinct clear lattice spacing of 0.204 nm for Fe (101) plane of Cu_3Fe is well resolved, which is 2% larger than that of pure Fe, indicating lattice stretching of Fe (101) Meanwhile, energy dispersive X-ray (EDS) elemental mapping analysis demonstrates the uniform distribution of Cu and Fe in the Cu_3Fe nanoalloy (Figure 1c). The percentages of each element is presented by an EDS mapping sum spectrum, and the detected Cu/Fe ratio of Cu_3Fe is close to 3/1, which is the initial starting material proportion, indicating that the mechanical milling method can retain an atomic ratio consistency (Figure S3).



Scheme 1. A schematic illustration explaining why Bulk Na cannot be pulverized by mechanical milling (**a**) while the mixture of Na, $CuCl_2$ and $FeCl_3$ can be converted to Cu-Fe cluster by mechanical milling (**b**).

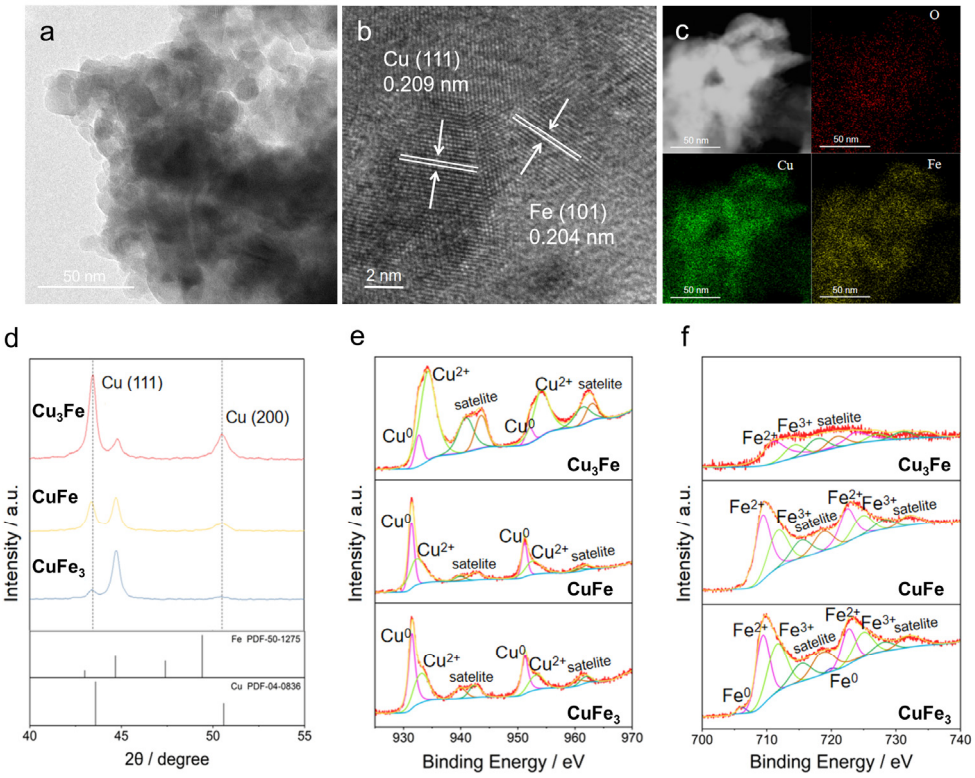


Figure 1. (**a**) TEM image (**b**) HRTEM image (**c**) EDS mapping image of Cu_3Fe; (**d**) XRD patterns (**e**) XPS Cu 2p spectra (**f**) XPS Fe 2p spectra of the Cu_3Fe, CuFe and $CuFe_3$, respectively.

XPS analysis is further performed to study the surface composition and chemical state of the sample. The survey spectra of the as-prepared samples confirm the presence of Cu, Fe and O in all the samples (Figure S4). Noteworthily, the strong O signal suggests that all the Cu-Fe nanoalloys involve surface oxidation. As shown in Figure 1e, two typical peaks located at 933.8 and 953.7 eV are resolved, corresponding to Cu^{2+} of Cu $2p_{3/2}$ and Cu $2p_{1/2}$ in Cu_3Fe, along with the other two satellite peaks. Another two characteristic peaks

centered at 932.5 and 951.9 eV are attributed to Cu^0 of Cu $2p_{3/2}$ and Cu $2p_{1/2}$ in Cu_3Fe. The plain Cu prepared through the same condition shows a characteristic peak at 932.7 eV for Cu^0 and a characteristic peak at 934.0 eV for Cu^{2+} (Figure S5). The result shows a 0.2 eV negative shift on Cu^0 species characteristic peaks and a positive shift on Cu^{2+} species characteristic peaks, indicating the electron transfer takes place at CuO/Cu interface [15]. In addition, a broad Fe 2p peak corresponding to the oxidized state is observed in Figure 1f. With the increase of Fe content, a negative shift of the Cu 2p peaks takes place, and the ratio of Cu^{2+}/Cu^0 decreases, indicating that introduction of Fe could effectively reduce Cu^{2+} and further regulate the electron structure between Cu^0 and Cu^{2+}, while strong Fe 2p peaks at 709.4 eV and 711.9 eV are resolved in CuFe and $CuFe_3$, suggesting the intensified oxidation and the electronic density decrease of Fe [16,17] (Figure 1f). The above XPS results demonstrate that the addition of Fe could effectively regulate the distribution of Cu 3d band, leading to the high electron density of Cu^0, which induces the decrease of reaction barrier and suppresses the competitive H_2 production, resulting in a high conversion rate, Faradaic efficiency (FE) and NH_3 selectivity for NRA [18–22].

The electrochemical denitrification performances of the as-prepared Cu-Fe nanoalloy samples are conducted based on a standard three-electrode system. All the reported potentials are converted to a reversible hydrogen electrode (RHE) scale. The nitrate removal rate is compared via electrolysis test at 0.7 V vs. RHE, Cu_5Fe, Cu_3Fe, CuFe and $CuFe_3$ shows a higher nitrate conversion than Fe and Cu prepared under the same condition (Figure 2a). It is worth noting that Cu_3Fe, CuFe and $CuFe_3$ show more effective electroreduction of nitrate than Cu_5Fe, thus pointing out the direction for the experiments subsequently. Cyclic voltammetry (CV) tests are carried out on Cu_3Fe, CuFe and $CuFe_3$ to compare their NRA activity in the electrolyte of 0.1 M Na_2SO_4 and 100 ppm NO_3^--N (Figure 2b). Compared with CuFe and $CuFe_3$, Cu_3Fe exhibits a much larger peak current density, indicating its highest intrinsic activity for catalyzing nitrate reduction. Cu_3Fe shows a greater current density in the electrolyte that contains nitrite than in the electrolyte containing nitrate, with 0.1 M Na_2SO_4 as the supporting electrolyte (Figure S6). Potentiostatic electrolysis test is conducted at −0.7 V vs. RHE. The reactant and reductive products, including nitrite and ammonia, are detected according to UV–Vis spectrophotometry results [23] (Figures 2c and S1). Continuous nitrate decrease takes place after electrolysis at different times on Cu_3Fe, CuFe and $CuFe_3$. Compared with CuFe and $CuFe_3$, Cu_3Fe shows the highest ammonium selectivity and nitrate conversion efficiency. The conversion of nitrate and the selectivity for ammonium on Cu_3Fe reaches 81.1% and 70.3% after 6 h (Figure 2c), respectively, which is comparable or even superior to most reported Cu-based nonnoble bimetallic catalysts [24,25]. The catalytic activity of Cu_3Fe for NRA is investigated under 0.1 M Na_2SO_4 with various concentrations of nitrate (Figure 2d). The significant current increase takes place with the rise of the NO_3^- concentration, showing the stepwise activation of Cu_3Fe.

Electrochemical transformation of nitrate into NH_4^+ involves complex proton-coupled electron transfer (PCET) reactions, which always compete with hydrogen evolution reaction (HER) [26]. Thus, controllable generation of highly reactive H plays a vital role in boosting NRA. According to previous research results, Fe-based materials are identified to be an efficient catalyst for the generation of H [7]. To verify the effect of Fe doping on boosting PCET, linear sweep voltammetry (LSV) characterization is performed on Cu-Fe nanoalloys with different Fe contents under 0.1 M KOH (Figure 2e). Obviously, the reduction current density grows with the content increase of Fe. The corresponding Tafel slope plots are depicted in Figure 2f; $CuFe_3$ exhibits the smallest Tafel slope of 0.29 V dec^{-1}, suggesting that the introduction of Fe is beneficial for boosting the apparent catalytic reaction kinetics. However, excess Fe introduction is detrimental to the nitrate conversion efficiency and NH_4^+ selectivity (Figure 2c). Therefore, it is reasonable to deduce that the greatly enhanced reduction current density and apparent reaction kinetics on Fe-rich nanoalloys are mainly triggered by the boosted HER. Generally, Cu plays a vital role in nitrate adsorption and subsequent reduction into nitrite, but it is insufficient for catalyzing following stepwise

reduction reactions during NRA [27–29]. Proper introduction of Fe into Cu is beneficial for promoting stepwise hydrogenation reactions of nitrite, while superfluous Fe will suppress NRA by covering the active sites of Cu and boosting the side HER reactions [30].

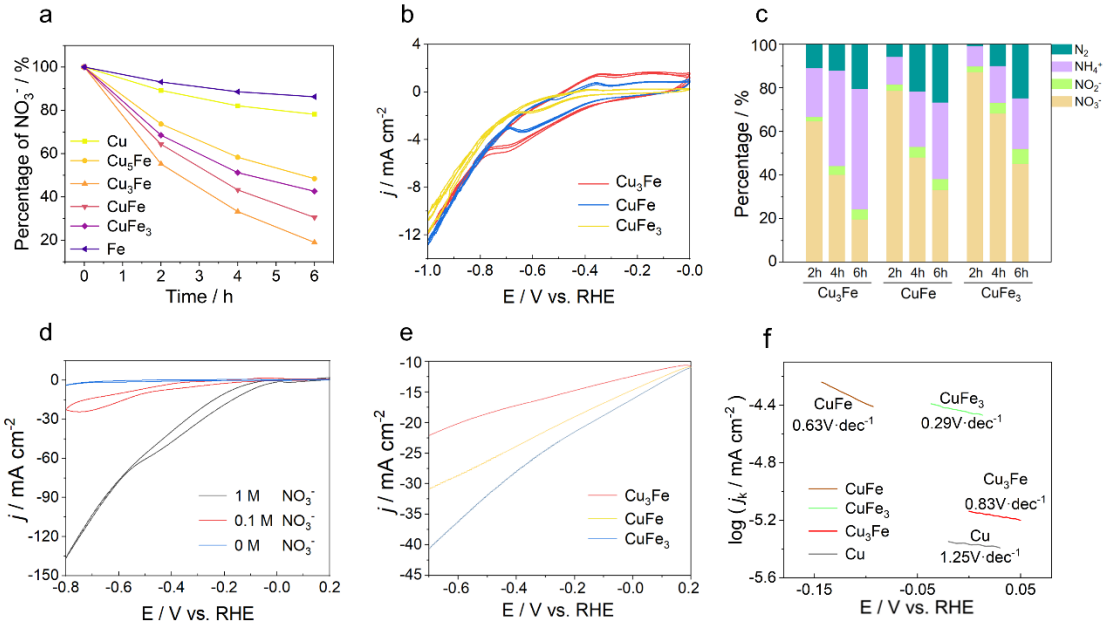


Figure 2. Electroreduction performance differences among catalysts. (**a**) The time-dependent concentration of nitrate compared among different Cu-Fe ratio catalysts in electrolysis test. (**b**) CV plots in an electrolyte of 100 ppm NO_3^--N and 0.1 M Na_2SO_4 of different catalysts. (**c**) Time-dependent product distributions of different catalysts. (**d**) CV plots of Cu_3Fe in electrolytes of different nitrate concentrations. Hydrogen evolution reaction (HER) performance. (**e**) LSV plots in 0.1 M NaOH among different catalysts prepared. (**f**) Tafel slope among different catalysts in 0.1 M NaOH.

To investigate electrocatalytic behaviors of the samples towards NRA, they are deposited on rotating disk electrodes (RDEs) and tested in a neutral electrolyte containing 0.1 M Na_2SO_4 and 0.01 M $NaNO_3$. A three-electrode configuration is applied with RDEs as the working electrode, and Pt wire and an Ag/AgCl electrode as counter electrode and reference electrode, respectively. Electrocatalytic behaviors of the Cu-Fe catalysts with different Fe contents were investigated. The half-wave potentials ($E_{1/2}$) of the catalysts towards electrocatalytic nitrate reduction were obtained from the LSV curves tested on RDEs (Figure 3a). It was observed that the Cu_3Fe exhibited the highest $E_{1/2}$ of −0.33 V vs. RHE, while the Cu possessed $E_{1/2}$ values of −0.37 V under the same testing conditions. The results indicated that Fe doping greatly enhanced NRA activity of the Cu catalysts [31]. In addition, an electrochemically active surface area (ECSA) test was conducted on Ni foam coated with Cu_3Fe and Cu, respectively. The result indicated that Cu_3Fe has greater intrinsic activity than Cu toward NRA, because Cu_3Fe presents a larger ECSA-normalized current density than Cu (Figure S7).

To determine the electron transfer number (n) of the Cu_3Fe and Cu in NRA, LSV curves of the RDEs at various rotating speeds were recorded (Figure 3b,c). The plain Cu catalyst was used as the control sample. The current density increased with increased rotation rate, owing to the shortened diffusion distance at high rotation speeds [32,33]. The corresponding Koutecky–Levich (K-L) plots at −0.7 V vs. RHE for the Cu_3Fe and plain Cu are shown in Figure 3d, which displays good linearity and near coincidence. The analysis of K-L equation revealed a 6-electron-transfer process for nitrate reduction on Cu_3Fe and an 8-electron-transfer process for nitrate reduction on plain Cu. Therefore, it is speculated that the reaction at −0.7 V vs. RHE on Cu_3Fe is the reduction of nitrite to ammonia, as the valence of N-containing species is reduced from +3 to –3 [5,34]. The nitrate-to-nitrite reduction potential was shifted positively because of the upshift of the *d*-band center (E_d).

The current density of Cu_3Fe was calculated based on the intercept of the K-L plot [35]. At an applied potential of −0.7 V vs. RHE, the kinetic current density of the Cu_3Fe is 46.3 mA cm^{-2}, which is 1.8 times that of the Cu catalyst (25.2 mA cm^{-2}), indicating the remarkably enhanced NRA activity of the Cu_3Fe (Table S1).

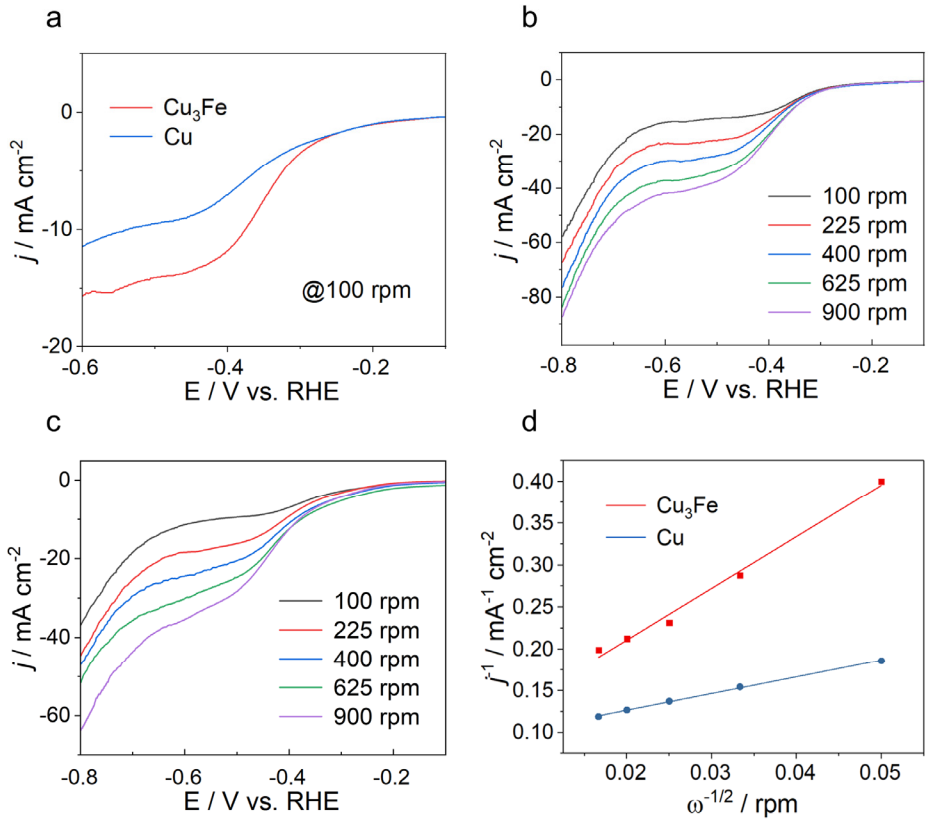


Figure 3. Electrocatalytic behavior of the CuFe catalyst towards nitrate reduction in 0.1 M Na_2SO_4 electrolyte with 0.01 M $NaNO_3$. (**a**) LSV curves of nitrate reduction on the Cu_3Fe and plain Cu-modified RDEs at 100 rpm without the ohmic potential drop compensation. (**b**) LSV curves of nitrate reduction on the Cu_3Fe-modified RDE at different rotation rates. (**c**) LSV curves of nitrate reduction on Cu-modified RDE at different rotation rates. (**d**) K-L plots of nitrate reduction on CuFe and Cu-modified RDEs at −0.7 V vs. RHE.

Electrolysis tests were conducted on Cu_3Fe to determine the most efficient potential which has the highest Faradaic efficiency (FE) for NRA (Figure 4a). The conversion of nitrate increased gradually as the potential rose from −0.6 V to −0.9 V vs. RHE, while the Faraday efficiency plot showed a volcanic curve with a maximum value of 74.2% at −0.7 V vs. RHE. Therefore, −0.7 V vs. RHE was selected as the test potential. With the extension of reaction time, the concentration of nitrate decreased while the concentration of ammonia increased, indicating the appearance of nitrate-to-ammonia electrochemical conversion (Figure 4d). After 5 cycles, the ammonia selectivity remained at a relatively high level, while the nitrate removal rate slightly decreased (Figure 4b). The degradation of nitrate removal rate may attribute to the excess loading of Cu-Fe nanoparticle on Ni foam for the weight of working electrode gradually decreased after 5 cycles of an electrocatalysis test. The effect of initial nitrate concentration on selectivity was investigated (Figure 4c). As the concentration of NO_3^--N increased from 100 ppm to 2000 ppm, the selectivity of ammonia remained almost unchanged, showing a wide range of applications. After 6 h of the electrocatalytic process, the morphology of the catalyst transferred from granular to flake (Figure S8).

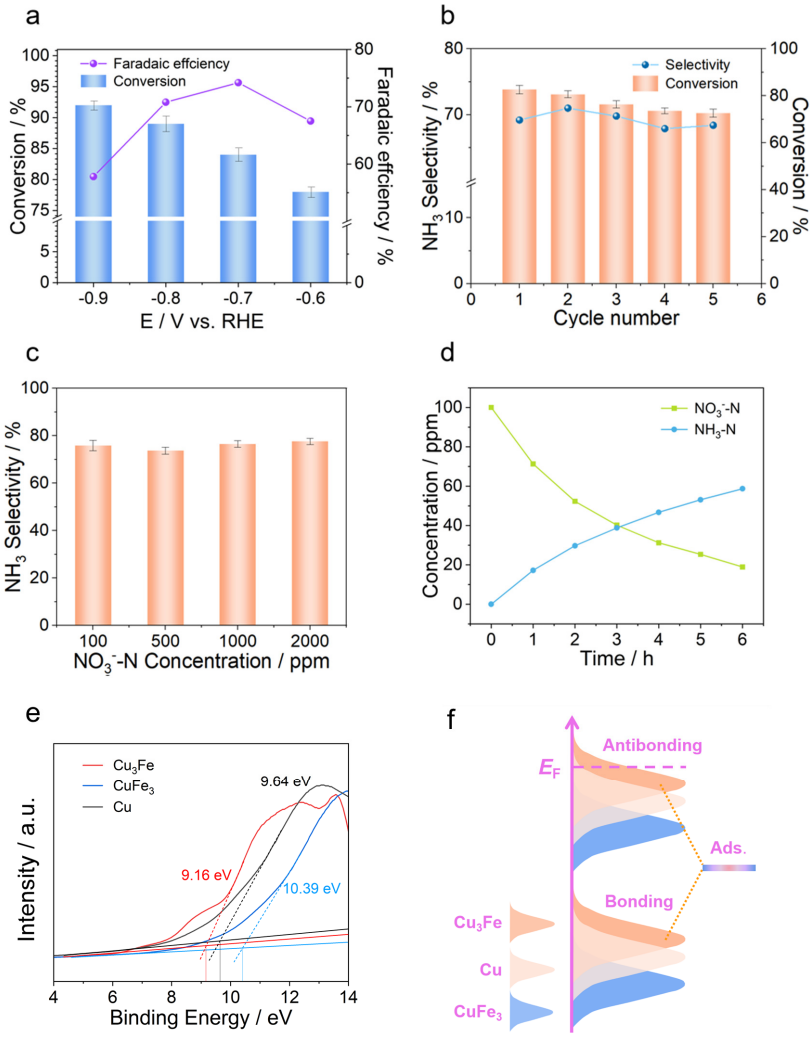


Figure 4. (**a**) Potential-dependent Faradaic efficiency of ammonia and conversion rate of nitrate over Cu_3Fe. (**b**) The consecutive recycling test at −0.7 V vs. RHE over Cu_3Fe cathode. (**c**) Selectivity of ammonia with different concentrations of nitrate over Cu_3Fe at −0.7 V vs. RHE. (**d**) The time-dependent concentration changes of NO_3^- and ammonia over Cu_3Fe at −0.7 V vs. RHE. (**e**) The ultraviolet photoelectron spectroscopy (UPS) plots of Cu_3Fe, $CuFe_3$ and Cu. (**f**) Schematic illustration of bond orbital variation between the catalysts with different Cu/Fe ratios and the adsorbates (Ads.).

According to the high-Resolution Transmission Electron Microscope (HRTEM) results (Figure 1b), the Cu (111) plane of Cu_3Fe nanoalloy exhibited a relatively larger lattice space than that of pure Cu nanoparticles. Crystal lattice expansion of Cu resulted in contraction and upshift of the corresponding d band energy level [36]. Generally, the *d*-band center (E_d) was considered a descriptor for the adsorbate-metal interaction [37,38]. When the catalyst surface chemically adsorbed nitrate and the corresponding intermediates, the *d*-band of Cu would couple with the energy level orbital of the adsorbates to form a bonding orbital and an anti-bonding orbital. The strength of chemical adsorption depended on the filling of the anti-bonding orbital. The up-shifted E_d of Cu_3Fe signifies the electron occupancy decrease of the anti-bonding orbital, and thus the interaction between the adsorbates and the surface of Cu_3Fe would be enhanced. In addition, the Fe catalyzed generation of reactive H was beneficial for the hydrogenation of the adsorbed oxynitrides. Hence, the adsorbed nitrite tended to be over hydrogenated to form ammonium, rather than falling off from the adsorption site to form nitrogen or other intermediate products [39].

To further explore the underlying electrocatalytic mechanism of the catalyst during RNA, ultraviolet photoelectron spectroscopy (UPS) was performed (Figure 4e). The position

of the *d*-band center was compared according to the value band maximum values of UPS, as shown in Figure 4 The valence band maximum values were calculated to be 9.16 eV, 9.64 eV and 10.39 eV for $CuFe_3$, Cu and $CuFe_3$, respectively. The valence band maximum (VBM) was shifted toward the Fermi level by moderate Fe-doping, while the opposite shift was observed after the excess of Fe content on $CuFe_3$. Since the valence electrons close to the Fermi level mainly contribute the d states [40,41], the shift of the valence band indicated the position of the *d*-band center also shifted (Figure 4f). It was found that the maximum value band of Cu_3Fe was 0.5 eV lower than that of Cu, indicating the corresponding upshift of E_d by 25% Fe-doping content, and the rearrangement of electron structure emerged in the presence of Fe-substituted.

4. Conclusions

In conclusion, Cu-Fe nanoparticles catalysts with flexible Cu/Fe ratios were successfully achieved simply through reactive mechanical milling strategy with metal chloride as the metal source and sodium as the reducing agent. Systematic structural and electrochemical analysis endorse that Fe introduction was beneficial for pushing up the *d*-band center of Cu_3Fe, resulting in greatly enhanced nitrate adsorption. Moreover, the intrinsic catalytic activity of Fe for the generation of H enabled stepwise hydrogenation reactions during nitrate reduction to make it more feasible and kinetically favorable. Benefitting from the unique structure, the optimized Cu_3Fe exhibited excellent electrocatalytic NRA performance under a neutral electrolyte. When the applied potential was −0.7 V vs. RHE, the kinetic current density provided by Cu_3Fe was recorded as 46.3 mA cm^{-2}, which is 1.8 times beyond that of Cu. In addition, a high Faraday efficiency of 74.2% and NH_4^+ selectivity of 70.3% was achieved under Cu_3Fe with great structure robustness. This study provides fundamental understanding and rational design strategies for developing highly efficient Cu-based electrocatalytic nitrate reduction catalysts.

Supplementary Materials: The following supporting information can be downloaded at: https://www.mdpi.com/article/10.3390/pr10040751/s1, Figure S1: The calibration curves of (a) nitrate-N, (b) nitrite-N, (c) ammonia-N for NO_3^- electroreduction and (d) the UV-Vis absorption spectra corresponding to ammonia-N with deionized water as background; Figure S2: The TEM images of (a,c) CuFe and (b,d) $CuFe_3$ nanoparticles; Figure S3: Element percentage of Cu_3Fe by EDS mapping sum spectrum results; Figure S4: XPS survey spectra of the (a) Cu3Fe, (b) CuFe and (c) CuFe3 nanoparticles; Figure S5: XPS Cu 2p of nano Cu catalyst prepared by ball-milling method; Figure S6: CV plots of different electrolyte by Cu_3Fe, 0.1 M Na_2SO_4 is used as background electrolyte for all the CV tests; Figure S7: ECSA-normalized current densities of Cu_3Fe and plain Cu catalysts measured by glassy carbon electrode in a 1 M NaOH electrolyte solution; Figure S8: The SEM images of Cu_3Fe catalyst (a) before and (b) after 6 h electrocatalysis test; Table S1: K-L analysis results of NO_3^- reduction on the Cu_3Fe and plain Cu catalysts in 10 mM NO_3^- and 0.1 M Na_2SO_4.

Author Contributions: Conceptualization, X.C. and Z.T.; methodology, Z.T.; software, X.L.; validation, Z.B. and X.L.; formal analysis, Z.T. and Z.B.; investigation, Z.T.; resources, X.L. and L.D.; data curation, Z.T.; writing—original draft preparation, Z.T.; writing—review and editing, X.C.; visualization, B.Z.; supervision, X.C.; project administration, X.C.; funding acquisition, L.D. All authors have read and agreed to the published version of the manuscript.

Funding: This work was supported by the Natural Science Foundation of China (No. 52101279), Natural Science Foundation of Hunan Provience (No. 2020JJ5688), Science Research Initiation Fund of Central South University (No. 202045012), Jiangsu Key Laboratory for Carbon-Based Functional Materials & Devices, Soochow University and the Fundamental Research Funds for the Central Universities of Central South University (No. 2020zzts753).

Institutional Review Board Statement: Not applicable.

Informed Consent Statement: Not applicable.

Data Availability Statement: Not applicable.

Acknowledgments: We are thankful to Central South University, Key Laboratory for Mineral Materials and Application of Hunan Province.

Conflicts of Interest: The authors declare that they have no known competing financial interests or personal relationships that could have appeared to influence the work reported in this paper.

References

1. Canfield, D.E.; Glazer, A.N.; Falkowski, P.G. The Evolution and Future of Earth's Nitrogen Cycle. *Science* **2010**, *330*, 192–196. [CrossRef]
2. Ascott, M.J.; Gooddy, D.C.; Wang, L.; Stuart, M.E.; Lewis, M.A.; Ward, R.S.; Binley, A.M. Global Patterns of Nitrate Storage in the Vadose Zone. *Nat. Commun.* **2017**, *8*, 1416. [CrossRef] [PubMed]
3. Tang, C.; Qiao, S.-Z. How to Explore Ambient Electrocatalytic Nitrogen Reduction Reliably and Insightfully. *Chem. Soc. Rev.* **2019**, *48*, 3166–3180. [CrossRef] [PubMed]
4. Yang, J.; Sebastian, P.; Duca, M.; Hoogenboom, T.; Koper, M.T.M. PH Dependence of the Electroreduction of Nitrate on Rh and Pt Polycrystalline Electrodes. *Chem. Commun.* **2014**, *50*, 2148–2151. [CrossRef]
5. Rosca, V.; Duca, M.; de Groot, M.T.; Koper, M.T.M. Nitrogen Cycle Electrocatalysis. *Chem. Rev.* **2009**, *109*, 2209–2244. [CrossRef] [PubMed]
6. Guo, Y.; Zhang, R.; Zhang, S.; Zhao, Y.; Yang, Q.; Huang, Z.; Dong, B.; Zhi, C. Pd Doping-Weakened Inter-mediate Adsorption to Promote Electrocatalytic Nitrate Reduction on TiO_2 Nanoarrays for Ammonia Production and Energy Supply with Zinc–Nitrate Batteries. *Energy Environ. Sci.* **2021**, *14*, 3938–3944. [CrossRef]
7. Liu, J.-X.; Richards, D.; Singh, N.; Goldsmith, B.R. Activity and Selectivity Trends in Electrocatalytic Nitrate Reduction on Transition Metals. *ACS Catal.* **2019**, *9*, 7052–7064. [CrossRef]
8. Wang, X.; Zhu, M.; Zeng, G.; Liu, X.; Fang, C.; Li, C. A Three-Dimensional Cu Nanobelt Cathode for Highly Efficient Electrocatalytic Nitrate Reduction. *Nanoscale* **2020**, *12*, 9385–9391. [CrossRef] [PubMed]
9. Soares, O.S.G.P.; Órfão, J.J.M.; Pereira, M.F.R. Activated Carbon Supported Metal Catalysts for Nitrate and Nitrite Reduction in Water. *Catal. Lett.* **2008**, *126*, 253–260. [CrossRef]
10. Wu, Z.-Y.; Karamad, M.; Yong, X.; Huang, Q.; Cullen, D.A.; Zhu, P.; Xia, C.; Xiao, Q.; Shakouri, M.; Chen, F.-Y.; et al. Electrochemical Ammonia Synthesis via Nitrate Reduction on Fe Single Atom Catalyst. *Nat. Commun.* **2021**, *12*, 2870. [CrossRef] [PubMed]
11. Gu, W.; Guo, Y.; Li, Q.; Tian, Y.; Chu, K. Lithium Iron Oxide ($LiFeO_2$) for Electroreduction of Dinitrogen to Ammonia. *ACS Appl. Mater. Interfaces* **2020**, *12*, 37258–37264. [CrossRef]
12. Kandemir, T.; Schuster, M.E.; Senyshyn, A.; Behrens, M.; Schlögl, R. The Haber-Bosch Process Revisited: On the Real Structure and Stability of "Ammonia Iron" under Working Conditions. *Angew. Chem. Int. Ed.* **2013**, *52*, 12723–12726. [CrossRef]
13. Liu, Z.; Chang, X.; Sun, B.; Yang, S.; Zheng, J.; Li, X. Room Temperature Solvent-Free Reduction of $SiCl_4$ to Nano-Si for High-Performance Li-Ion Batteries. *Chem. Commun.* **2017**, *53*, 6223–6226. [CrossRef] [PubMed]
14. Theivasanthi, T.; Alagar, M. X-Ray Diffraction Studies of Copper Nanopowder. *arXiv* **2010**, arXiv:1003.6068.
15. Dubot, P.; Jousset, D.; Pinet, V.; Pellerin, F.; Langeron, J.P. Simulation of the LMM Auger Spectra of Copper. *Surf. Interface Anal.* **1988**, *12*, 99–104. [CrossRef]
16. Tang, C.; Gan, L.; Zhang, R.; Lu, W.; Jiang, X.; Asiri, A.M.; Sun, X.; Wang, J.; Chen, L. Ternary Fe_x Co_{1-x} P Nanowire Array as a Robust Hydrogen Evolution Reaction Electrocatalyst with Pt-like Activity: Experimental and Theoretical Insight. *Nano Lett.* **2016**, *16*, 6617–6621. [CrossRef] [PubMed]
17. Wu, H.; Yang, T.; Du, Y.; Shen, L.; Ho, G.W. Identification of Facet-Governing Reactivity in Hematite for Oxygen Evolution. *Adv. Mater.* **2018**, *30*, 1804341. [CrossRef]
18. Wang, Y.; Zhou, W.; Jia, R.; Yu, Y.; Zhang, B. Unveiling the Activity Origin of a Copper-based Electrocatalyst for Selective Nitrate Reduction to Ammonia. *Angew. Chem. Int. Ed.* **2020**, *59*, 5350–5354. [CrossRef]
19. Chong, X.; Liu, C.; Huang, Y.; Huang, C.; Zhang, B. Potential-Tuned Selective Electrosynthesis of Azoxy-, Azo- and Amino-Aromatics over a CoP Nanosheet Cathode. *Natl. Sci. Rev.* **2020**, *7*, 285–295. [CrossRef]
20. Li, P.; Wang, M.; Duan, X.; Zheng, L.; Cheng, X.; Zhang, Y.; Kuang, Y.; Li, Y.; Ma, Q.; Feng, Z.; et al. Boosting Oxygen Evolution of Single-Atomic Ruthenium through Electronic Coupling with Cobalt-Iron Layered Double Hydroxides. *Nat. Commun.* **2019**, *10*, 1711. [CrossRef]
21. Song, F.; Li, W.; Yang, J.; Han, G.; Yan, T.; Liu, X.; Rao, Y.; Liao, P.; Cao, Z.; Sun, Y. Interfacial Sites between Cobalt Nitride and Cobalt Act as Bifunctional Catalysts for Hydrogen Electrochemistry. *ACS Energy Lett.* **2019**, *4*, 1594–1601. [CrossRef]
22. Tao, L.; Shi, Y.; Huang, Y.-C.; Chen, R.; Zhang, Y.; Huo, J.; Zou, Y.; Yu, G.; Luo, J.; Dong, C.-L.; et al. Interface Engineering of Pt and CeO_2 Nanorods with Unique Interaction for Methanol Oxidation. *Nano Energy* **2018**, *53*, 604–612. [CrossRef]
23. McCrady, M.H. Standard Methods for the Examination of Water and Waste-Water (12th Ed.). *Am. J. Public Health Nations Health* **1966**, *56*, 684. [CrossRef]
24. Wang, Q.; Huang, H.; Wang, L.; Chen, Y. Electrochemical Removal of Nitrate by Cu/Ti Electrode Coupled with Copper-Modified Activated Carbon Particles at a Low Current Density. *Environ. Sci. Pollut. Res.* **2019**, *26*, 17567–17576. [CrossRef] [PubMed]

25. Gao, W.; Gao, L.; Meng, J.; Li, D.; Guan, Y.; Cui, L.; Shen, X.; Liang, J. Preparation of a Novel Cu-Sn-Bi Cathode and Performance on Nitrate Electroreduction. *Water Sci. Technol.* **2019**, *79*, 198–206. [CrossRef]
26. He, D.; Li, Y.; Ooka, H.; Go, Y.K.; Jin, F.; Kim, S.H.; Nakamura, R. Selective Electrocatalytic Reduction of Nitrite to Dinitrogen Based on Decoupled Proton–Electron Transfer. *J. Am. Chem. Soc.* **2018**, *140*, 2012–2015. [CrossRef] [PubMed]
27. Roy, C.; Deschamps, J.; Martin, M.H.; Bertin, E.; Reyter, D.; Garbarino, S.; Roué, L.; Guay, D. Identification of Cu Surface Active Sites for a Complete Nitrate-to-Nitrite Conversion with Nanostructured Catalysts. *Appl. Catal. B Environ.* **2016**, *187*, 399–407. [CrossRef]
28. Çirmi, D.; Aydın, R.; Köleli, F. The Electrochemical Reduction of Nitrate Ion on Polypyrrole Coated Copper Electrode. *J. Electroanal. Chem.* **2015**, *736*, 101–106. [CrossRef]
29. Wu, T.; Kong, X.; Tong, S.; Chen, Y.; Liu, J.; Tang, Y.; Yang, X.; Chen, Y.; Wan, P. Self-Supported Cu Nanosheets Derived from CuCl-CuO for Highly Efficient Electrochemical Degradation of NO^{3-}. *Appl. Surf. Sci.* **2019**, *489*, 321–329. [CrossRef]
30. Lan, Y.; Luo, H.; Ma, Y.; Hua, Y.; Liao, T.; Yang, J. Synergy between Copper and Iron Sites inside Carbon Nanofibers for Superior Electrocatalytic Denitrification. *Nanoscale* **2021**, *13*, 10108–10115. [CrossRef] [PubMed]
31. Wang, C.; Liu, Z.; Hu, T.; Li, J.; Dong, L.; Du, F.; Li, C.; Guo, C. Metasequoia-like Nanocrystal of Iron-Doped Copper for Efficient Electrocatalytic Nitrate Reduction into Ammonia in Neutral Media. *ChemSusChem* **2021**, *14*, 1825–1829. [CrossRef] [PubMed]
32. Yang, H.B.; Guo, C.; Zhang, L.; Hu, F.X.; Cai, W.; Gao, J.; Li, C.M.; Liu, B. Nitrogen and Sulfur Co-Doped Graphene Inlaid with Cobalt Clusters for Efficient Oxygen Reduction Reaction. Mater. *Today Energy* **2018**, *10*, 184–190. [CrossRef]
33. Hu, F.; Yang, H.; Wang, C.; Zhang, Y.; Lu, H.; Wang, Q. Co-N-Doped Mesoporous Carbon Hollow Spheres as Highly Efficient Electrocatalysts for Oxygen Reduction Reaction. *Small* **2017**, *13*, 1602507. [CrossRef]
34. Garcia-Segura, S.; Lanzarini-Lopes, M.; Hristovski, K.; Westerhoff, P. Electrocatalytic Reduction of Nitrate: Fundamentals to Full-Scale Water Treatment Applications. *Appl. Catal. B Environ.* **2018**, *236*, 546–568. [CrossRef]
35. Wang, Y.; Xu, A.; Wang, Z.; Huang, L.; Li, J.; Li, F.; Wicks, J.; Luo, M.; Nam, D.-H.; Tan, C.-S.; et al. Enhanced Nitrate-to-Ammonia Activity on Copper–Nickel Alloys via Tuning of Intermediate Adsorption. *J. Am. Chem. Soc.* **2020**, *142*, 5702–5708. [CrossRef] [PubMed]
36. Esterhuizen, J.A.; Goldsmith, B.R.; Linic, S. Theory-Guided Machine Learning Finds Geometric Struc-ture-Property Relationships for Chemisorption on Subsurface Alloys. *Chem* **2020**, *6*, 3100–3117. [CrossRef]
37. Hsieh, H.H.; Chang, Y.K.; Pong, W.F.; Pieh, J.Y.; Tseng, P.K.; Sham, T.K.; Coulthard, I.; Naftel, S.J.; Lee, J.F.; Chung, S.C.; et al. Electronic Structure of Ni-Cu Alloys: The d -Electron Charge Distribution. *Phys. Rev. B* **1998**, *57*, 15204–15210. [CrossRef]
38. Chu, K.; Gu, W.; Li, Q.; Liu, Y.; Tian, Y.; Liu, W. Amorphization Activated FeB_2 Porous Nanosheets Enable Efficient Electrocatalytic N_2 Fixation. *J. Energy Chem.* **2021**, *53*, 82–89. [CrossRef]
39. Wei, L.; Liu, D.-J.; Rosales, B.A.; Evans, J.W.; Vela, J. Mild and Selective Hydrogenation of Nitrate to Am-monia in the Absence of Noble Metals. *ACS Catal.* **2020**, *10*, 3618–3628. [CrossRef]
40. Chen, Z.; Song, Y.; Cai, J.; Zheng, X.; Han, D.; Wu, Y.; Zang, Y.; Niu, S.; Liu, Y.; Zhu, J.; et al. Tailoring the D-Band Centers Enables Co_4N Nanosheets to Be Highly Active for Hydrogen Evolution Catalysis. *Angew. Chem. Int. Ed.* **2018**, *57*, 5076–5080. [CrossRef] [PubMed]
41. Song, Q.; Li, J.; Wang, S.; Liu, J.; Liu, X.; Pang, L.; Li, H.; Liu, H. Enhanced Electrocatalytic Performance through Body Enrichment of Co-Based Bimetallic Nanoparticles In Situ Embedded Porous N-Doped Carbon Spheres. *Small* **2019**, *15*, 1903395. [CrossRef] [PubMed]